Author/s:
Castelli, M;Hellerstedt, J;Krull, C;Gicev, S;Hollenberg, LCL;Usman, M;Schiffrin, A

Title:
Long-Range Surface-Assisted Molecule-Molecule Hybridization

Date:
2021-03-01

Citation:
Castelli, M., Hellerstedt, J., Krull, C., Gicev, S., Hollenberg, L. C. L., Usman, M. & Schiffrin, A. (2021). Long-Range Surface-Assisted Molecule-Molecule Hybridization. Small, 17 (10), https://doi.org/10.1002/smll.202005974.

Persistent Link:
https://hdl.handle.net/11343/298228

Long-Range Surface-Assisted Molecule-Molecule Hybridization

Marina Castelli, Jack Hellerstedt, Cornelius Krull, Spiro Gicev, Lloyd C.L. Hollenberg, Muhammad Usman, Agustin Schiffrin**

Dr. M. Castelli, Dr. J. Hellerstedt, Dr. C. Krull, Dr. A. Schiffrin

School of Physics and Astronomy, Monash University, Clayton, Victoria 3800, Australia

Email: agustin.schiffrin@monash.edu

Dr. M. Castelli, Dr. C. Krull, Dr. A. Schiffrin

ARC Centre of Excellence in Future Low-Energy Electronics Technologies, Monash University, Clayton, Victoria 3800, Australia

S. Gicev, Dr. M. Usman, Prof. L.C.L Hollenberg

Centre for Quantum Computation and Communication Technology, School of Physics, The University of Melbourne, Parkville, 3010, Victoria, Australia

Email: muhammad.usman@unimelb.edu.au

Dr. M. Usman

School of Computing and Information Systems, Melbourne School of Engineering, The University of Melbourne, Parkville, 3010, Victoria, Australia

Keywords: scanning tunneling microscopy and spectroscopy, non-contact atomic force microscopy, density functional theory, intermolecular interactions, metal-organic complexes, surface chemistry.

This is the author manuscript accepted for publication and has undergone full peer review but has not been through the copyediting, typesetting, pagination and proofreading process, which may lead to differences between this version and the Version of Record. Please cite this article as doi: 10.1002/smll.202005974.

Abstract: Metalated phthalocyanines (Pc's) are robust and versatile molecular complexes, whose properties can be tuned by changing their functional groups and central metal atom. The electronic structure of magnesium Pc (MgPc) - structurally and electronically similar to chlorophyll – adsorbed on the Ag(100) surface is investigated by low-temperature scanning tunneling microscopy (STM) and spectroscopy (STS), non-contact atomic force microscopy (ncAFM) and density functional theory (DFT). Single, isolated MgPc's exhibit a flat, four-fold rotationally symmetric morphology, with doubly degenerate, partially populated (due to surface-to-molecule electron transfer) lowest unoccupied molecular orbitals (LUMOs). In contrast, MgPc's with neighbouring molecules in proximity undergo a lift of LUMOs degeneracy, with a near-Fermi local density of states with reduced two-fold rotational symmetry, indicative of a long-range attractive intermolecular interaction. The latter is assigned to a surface-mediated two-step electronic hybridization process. First, LUMOs interact with Ag(100) conduction electrons, forming hybrid molecule-surface orbitals with enhanced spatial extension. Then, these delocalized molecule-surface states further hybridize with those of neighbouring molecules. This work highlights how the electronic structure of molecular adsorbates – including orbital degeneracies and symmetries – can be significantly altered via surface-mediated intermolecular hybridization, over extended distances (beyond 3 nm), having important implications for prospects of molecule-based solid-state technologies.

1. Introduction

Tetrapyrrole molecules – in particular phthalocyanines (Pc's) and porphyrins – with single coordinated metal atoms at their core allow for a vast range of applications in, e.g., catalysis[1, 2], photovoltaic devices[3-5], light-emitting devices[6-8], molecular magnets[9-11], molecular rotors[12], nanoelectronics[13], gas sensing[14], molecular switches[15]. These functionalities are dictated by the electronic structure at the single molecule level[16-18]. Systems of practical interest are generally composed of many molecules, and their overall electronic character can be affected by intermolecular interactions (e.g., covalent, non-covalent, electrostatic, magnetic). Moreover, solid-state technologies based on such compounds require interfacing with a solid surface, which can further perturb their electronic properties. It is therefore of fundamental and technological importance to develop an in-depth understanding of the electronic structure of such metal-organic systems, in particular of their interactions with an underlying solid as well as with other adsorbates.

The morphology of neutral, non-interacting metal-porphyrins and metal-Pc's (M-Pc's) is natively planar, with four-fold rotational symmetry, and mirror symmetry planes along the isoindole-isoindole molecular axes and perpendicular to the molecular plane[17, 18]. Their electronic structure is characterised by two degenerate lowest unoccupied molecular orbitals (LUMOs) with strong (if not dominant) contributions from the organic Pc ligand[19]. When adsorbed on a solid surface, in some instances, these structural and electronic molecular symmetries can be maintained[10, 20-22]. In other cases, these can be broken via anisotropic

electronic interactions with the underlying substrate[23-26] or with other adsorbates[27, 28]. Such a break of symmetry can be accompanied by a lift of the LUMOs degeneracy[26-28]. Upon adsorption, the doubly degenerate LUMOs can become partially occupied due to surface-to-molecule electron transfer which can lift the degeneracy via Jahn-Teller (JT) distortion, stabilizing the extra negative charge and reducing the rotational symmetry from four- to two-fold[26, 27, 29, 30].

Scanning tunnelling microscopy (STM) and differential conductance (dI/dV) scanning tunnelling spectroscopy (STS [31]) allow for addressing and correlating changes in morphology and electronic structure of adsorbed molecules with intramolecular real-space resolution. However, phenomena such as surface-to-molecule charge transfer, Kondo effect[10, 24, 32, 33], lifts of orbital degeneracies due to JT distortion, and molecular vibrational modes, often give rise to dI/dV STS signatures at or near the Fermi level (within an energy window typically on the order of tens of meV[28, 34-36]). This can make it challenging to disentangle and fully understand these different physical phenomena.

Because of their potential magnetic functionality, adsorbed M-Pc's with *d*-block transition metal atoms at their core (e.g., NiPc, FePc, CuPc, ZnPc, CoPc) have been studied extensively by STM and dI/dV STS, in particular on noble metal (100) surfaces, where they preserve their structural and electronic, four-fold rotational symmetry[10, 23, 37]. Adsorbed M-Pc's with a simpler electronic structure (e.g., with *s*-block transition metal atoms at their core, lacking *d*-electrons) can make it easier to disentangle these contributions but remain underexplored. For instance, a detailed STM/STS characterisation of the atomic-scale morphology and electronic structure of the *s*-block magnesium Pc (MgPc[19]) – similar to chlorophyll[38] and with potential for light-harvesting and light-emitting technologies[5, 39, 40] – adsorbed on a noble metal (100) surface has not been performed to our knowledge.

Here we show by means of low-temperature STM, dI/dV STS, non-contact atomic force microscopy (ncAFM) and density functional theory (DFT), that single MgPc molecules on Ag(100) are four-fold rotationally symmetric with doubly degenerate and partially populated LUMOs, similar to other M-Pc's[10, 23, 28, 32-34]. However, when another MgPc is in proximity (for intermolecular distances up to ~3 nm), the LUMOs degeneracy can be lifted and the near-Fermi LDOS can exhibit a reduced two-fold rotational symmetry. We explain our observations by a two-step electronic hybridization process resulting in an effective long-range attractive molecule-molecule interaction, where: (i) the degenerate LUMOs of an MgPc molecule interact with Ag(100) conduction electron states, forming hybrid molecule-surface orbitals with enhanced spatial extension; (ii) these delocalized hybrid molecule-surface orbitals associated with a pair of nearest-neighbouring molecules can hybridize in turn. This work reports a first experimental evidence and detailed theoretical understanding of long-range substrate-mediated molecule-molecule electronic hybridisation, resulting in an effective attractive intermolecular interaction which survives beyond distances of ~3 nm. Such interaction could have important implications in the design of prospective molecule-based solid-state technologies.

2. Results

2.1 Structural Characterization of MgPc on Ag(100): STM, ncAFM and DFT

We deposited MgPc molecules onto a clean Ag(100) surface via thermal evaporation (see Methods). We subsequently characterised the MgPc/Ag(100) system via low-temperature (4.6 K) STM. **Figure 1a** shows an STM topographic image of molecules appearing as cross-like features, characteristic of the phthalocyanine (Pc) ligand[41-43]. The molecules adsorb with their isoindole-isoindole axes (green and magenta dashed lines in Figure 1a) following a ±29 ± 1° angle with respect to the [011] crystalline directions of Ag(100), consistent with previous studies[10, 23]. We identified two types of MgPc's on the Ag(100) surface. The first type labelled "single" has the four-fold rotational symmetry and mirror symmetry planes along the isoindole-isoindole axes inherited from the gas phase, as shown in the apparent height profiles (solid magenta and green curves) in Figure 1a. The second type consists of MgPc's whose low-bias STM topography, in contrast with the "single" molecules, reveals a reduced two-fold rotational symmetry, with two mirror-symmetric isoindole groups having an apparent height larger than those along the other orthogonal isoindole-isoindole axis (see height profile differences in Figures 1b, c). Notably, we observed this reduction of symmetry for MgPc's that are in proximity of another MgPc molecule, with their lowest-apparent-height isoindole-isoindole axis collinear to the axis defined by the two Mg-Mg centers. We named such pairs of nearest-neighbour MgPc's with collinear isoindole-isoindole axis "++" dimers (orange frame in Figure 1a).

To quantify the break of molecular symmetry observed in STM topography, we defined a topographic asymmetry parameter, $\alpha_{\mathrm{STM}} = \frac{|(z_1+z_3)-(z_2+z_4)|}{z_1+z_3+z_2+z_4}$, where z_j (j = 1,…, 4) is the maximum STM apparent height of each of the four isoindole units of a molecule (such that $z_1 > z_3 > z_2 > z_4$). Figure 1d shows α_{STM} for a single isolated MgPc (blue) and for MgPc of a "++" dimer (Mg-Mg distance $d_{\mathrm{c\text{-}c}}$ = 2.1 nm; orange) as a function of applied bias voltage V_{b}. For the single MgPc, α_{STM} is close to zero and independent of V_{b}. The "++" dimer is qualitatively different, with α_{STM} peaking at V_{b} = 0.02 V and attenuating symmetrically [see Figure S3 in Supporting Information (SI)].

In order to determine whether this reduction of STM rotational symmetry is due to a change in intramolecular morphology, we performed frequency-shift (Δf) ncAFM measurements with a carbon-monoxide (CO)-functionalized tip (Methods), on a single MgPc (**Figure 2a**) and a "++" dimer (Figure 2b). This technique enables real-space intramolecular structural characterisation with chemical bond resolution[44, 45]. Both the single molecule and "++" dimer cases show very similar four-fold rotationally symmetric morphologies, with the four distinguishable isoindole units identical to their Lewis structure. The Mg centers of both configurations show a "hash"-shaped appearance, where the four nitrogen (N) atoms of the pyrrole rings seem interconnected. The latter could be explained by the flexibility and dipole moment of the CO tip, known to introduce artefacts[46, 47]. Similar imaging was reported for FePc[48], attributed to a lowered density of electrons at the metal centre. Importantly, constant-height Δf profiles along the isoindole-isoindole axes (solid green and magenta

curves in Figures 2a, b) corroborate that the intramolecular morphology of MgPc remains the same (within our experimental resolution) for both single and "++" dimer configurations. We performed DFT calculations to determine the theoretical lowest-energy (relaxed) morphology of the single isolated MgPc and of the "++" dimer on the Ag(100) surface (Figures 2c, d; see Methods for computational details). These calculations show that, in both cases, the intramolecular conformation is quasi-identical, with the central Mg atom sitting on top of a Ag(100) hollow site, and with molecular height differences of, at most, ~3 pm (smaller than our experimental error). This agrees with our STM and ncAFM data (Figures 2a, b; SI Figures S1, S2), and with previously reported studies of other M-Pc's on (100) noble metal surfaces[10, 23, 37]. Combined with the bias voltage dependence of α_{STM} (Figure 1d), we conclude that the observed break of STM topography symmetry is not due to a different adsorption site of the molecule, nor to an intramolecular structural deformation; it is exclusively the result of changes in the molecular near-Fermi electronic structure induced by interactions with a neighbouring molecule.

2.2 Electronic Structure of MgPc on Ag(100): d*I*/d*V* STS and DFT

To elucidate the electronic structure of both single MgPc and MgPc in "++" dimers, we performed differential conductance (d*I*/d*V*) STS measurements (Methods). **Figure 3** contains d*I*/d*V* point spectra taken at the periphery of the Pc ligand (blue) and on the Mg center (red), for both single MgPc (triangles) and "++" dimer (squares). In both single MgPc and dimer cases, we identified prominent features at V_b = -1.45 and 2.8 V. Given that these bias voltages are far from that at which α_{STM} is maximum (Figure 1d), we conclude that the electronic states associated with these features play no role in the break of molecular topographic symmetry observed in Figure 1 (see SI Section S5 and Supplementary Figure S7 for details on the spatial distribution of these far-from-Fermi resonances).

At small absolute values of bias voltage, d*I*/d*V* spectra for both the single MgPc and "++" dimer show, at the Mg center, step-like features (red arrows in Figure 3) symmetric in energy with respect to the Fermi level (V_b = 0), and a sharp resonance at ~ -0.1 V on the Pc ligand. In **Figures 4** and 5 we focus on these near-Fermi spectroscopic features. Note that we did not observe any Kondo-effect-related zero bias peak or dip. We fit (Figure 4a) the central Mg-related spectra with a sum of an attenuated reference spectrum taken on bare Ag(100) (to account for tip features), and three pairs of Fermi-Dirac distributions symmetric with respect to V_b = 0, with onsets at ±0.005 ± 0.001, ±0.089 ± 0.001 and ±0.2 ± 0.001 V (see SI section S6 for details on fitting). Given their step-like near-Fermi character and their symmetry with respect to the Fermi level, we attribute these features to inelastic contributions to the differential conductance given by molecular vibrational modes associated with the Mg-N bonds and stretching of the isoindole units. This is consistent with previous studies of MgPc and other M-Pc's[34, 49, 50]. The d*I*/d*V* maps at V_b = ±0.2 V in Figures 4b-e, associated with the spatial distributions of these vibrational step-like features, are qualitatively identical for both single (Figures 4b, c) and dimer (Figures 4d, e), with symmetries that do not correspond to the topographic changes observed in Figure 1. Therefore, we conclude that the break of symmetry observed in Figure 1 is not related to these vibrational d*I*/d*V* features. We ascribe the variations in d*I*/d*V* signal around the molecular periphery observed in these d*I*/d*V* maps at

V_b= ±0.2 V (Figures 4b-e) to tip asymmetries which could be exacerbated by the multipass measurement technique (SI section S7).

The blue curve in **Figure 5a** corresponds to the dI/dV spectrum at the peripheral Pc ligand of a single MgPc (averaged over areas indicated by dashed blue circles in Figure 5b). Similar to the Mg center, we fit this dI/dV spectrum with a pair of energy-symmetric Fermi-Dirac distributions (onsets at ±0.202 ± 0.001 V; related to the most prevalent vibrational mode) and a Gaussian peak (centered at –0.097 ± 0.001 V). The dI/dV map associated with this Gaussian peak (Figure 5b), with predominant intensity at the peripheral Pc, shows regions with vanishing intensity along the axes defined by two opposite isoindole groups (grey arrows). This experimental map is similar to the simulated dI/dV map derived from DFT calculations (Methods), at an energy related to the doubly degenerate (populated) MgPc/Ag(100) LUMOs (Figure 5f), where each LUMO extends along two opposite isoindole groups, with two nodal planes (grey arrows) orthogonal to the molecular plane and to each other, along the isoindole-isoindole axes [43] (see SI Figure S18). Therefore, we attribute the Gaussian peak at ~ -97 mV in Figure 5a to the doubly degenerate gas-phase LUMOs. The nodal planes indicated by grey arrows reflect the symmetries of the corresponding molecular orbitals: the dI/dV map in Figure 5b associated with these LUMOs, with its two nodal planes, is four-fold rotationally symmetric.

The Gaussian peak associated with the LUMOs crosses the Fermi level, indicative of partial filling of the LUMOs due to Ag(100)-to-MgPc electron transfer. Bader charge analysis[51] based on our DFT calculations estimates that ~1.3 electrons are transferred to MgPc upon adsorption, in agreement with previous work[10]. The symmetry of this dI/dV map in Figure 5b indicates that the transferred negative charge populates each of the two LUMOs with equal probability, and that adsorption on Ag(100) does not lift the LUMOs degeneracy.

In the "++" dimer configuration, the Pc ligand dI/dV spectra (orange and green curves in Figure 5a) are similar to that for single MgPc. However, they present subtle differences depending on the exact acquisition location (orange and green dashed circles in Figures 5d, e). Whilst we were able to fit well the orange spectrum in Figure 5a with a pair of Fermi-Dirac distributions (onsets at ±0.198 ± 0.001 V; vibrational mode) and a Gaussian peak (-0.098 ± 0.001 V), the green spectrum required the addition of an extra Gaussian peak at 0.157 ± 0.002 V (see SI Section S6). Figures 5d, e show dI/dV maps associated with these Gaussian peaks, at -0.08 and 0.15 V, respectively. The map at 0.15 V was subtracted by the dI/dV map at 0.08 V (i.e., $\Delta(\mathrm{d}I/\mathrm{d}V)_{(0.15\ \mathrm{V};\ 0.08\ \mathrm{V})} = (\mathrm{d}I/\mathrm{d}V)_{0.15\ \mathrm{V}} - (\mathrm{d}I/\mathrm{d}V)_{0.08\ \mathrm{V}}$), in order to attenuate inelastic contributions from molecular vibrational modes (which dominate the spectra near Fermi; Figures 4c, e) and enhance peripheral Pc ligand features related to the Gaussian peak. The dI/dV map at -0.08 V in Figure 5d exhibits only one nodal plane parallel to the Mg-Mg dimer axis. The dI/dV map at +0.15 V in Figure 5e shows only one nodal plane perpendicular to this Mg-Mg axis. Based on these nodal planes, each of these two dI/dV maps is qualitatively identical to its rotation by 180° with respect to an axis going through the Mg center perpendicular to the surface. That is, the dI/dV maps of MgPc in the "++" dimer at -0.08 and +0.15 V have each two-fold rotational symmetry. The dI/dV map at -0.08 V of a

molecular in the "++" dimer, rotated by 90°, is qualitatively identical to that at 0.15 V for the same molecule. This is in stark contrast to a single MgPc (Figure 5b), with its two nodal planes (four-fold symmetry). We attribute the two Gaussian peaks in the green dI/dV spectrum in Figure 5a, and their associated reduced spatial symmetry (from four-fold rotational to two-fold rotational, i.e., from two nodal planes to only one; Figures 5d, e), to the two LUMOs, with their degeneracy lifted by interactions with the neighbouring molecule in the "++" dimer. One LUMO is occupied (-0.08 V); the other one is empty (0.15 V). This reduction of orbital rotational symmetry (i.e., reduction of nodal plane number) and lift of LUMOs degeneracy is the cause of the break of symmetry observed in the STM topography in Figure 1. This is consistent with DFT-simulated dI/dV maps of the "++" dimer (Figures 5h, i), which reveal near-Fermi occupied and empty electronic states, associated with the LUMOs, each with one nodal plane perpendicular to that of the other (that is, each LUMO with a two-fold rotationally symmetric spatial distribution orthogonal to that of each other). To address the influence of the noble metal substrate, we used DFT to calculate differential conductance maps of a neutral MgPc "++" dimer in the gas phase, at energies related to the (here unoccupied) LUMOs (see SI Figure S20). We observed a similar lift of degeneracy and reduction of rotational symmetry of the LUMOs, but only for small ($d_{c\text{-}c} < 2$ nm) Mg-Mg intermolecular distances. We therefore infer that the extended spatial range of the intermolecular interaction on Ag(100) is surface mediated.

Similar phenomena have been observed previously for other M-Pc's with partially filled LUMOs (i.e., negatively charged) on metals and atomically thin insulators, where degeneracy lifting and rotational symmetry reduction were induced by Jahn-Teller distortions mediated by inhomogeneous or anisotropic interactions with the substrate [26, 43] or neighbouring adatoms[27]. In the latter case, the molecule-adatom interaction was repulsive, resulting in the lowest-energy LUMO nodal plane being perpendicular to the axis defined by the M-Pc center and the adatom. In our "++" dimer case, we observe the opposite: the lowest-energy LUMO nodal plane is parallel to the Mg-Mg dimer axis (Figure 5d), whereas the nodal plane of the high energy LUMO (Figure 5e) is perpendicular to this axis. This indicates that the interaction between the MgPc molecules in the "++" dimer is effectively attractive (see SI Figure S17), despite their identical (negative) charge. The dI/dV map at 0.15 V for a single isolated MgPc (Figure 5c) hints towards the presence of two orthogonal nodal planes (grey arrows). This is qualitatively similar to the dI/dV map at -0.08 V related to the degenerate LUMOs (Figure 5b). Note that the non-optimal dI/dV signal contrast in Figure 5c could be explained by the subtraction by the 0.08 V dI/dV map (performed to attenuate contributions from molecular vibrational modes, as above).

We understand the comparable nodal plane assignment and symmetries between the -0.08 and 0.15 V maps as a consequence of the partial filling of the doubly degenerate LUMOs, and of the Hubbard energy U necessary to overcome the Coulomb repulsion when injecting a tunneling electron into these[34] (i.e., for $V_b > 0$). The 0.15 V map can be interpreted as a residue (tail) of a possible LUMO+U spectroscopic feature at higher energy (see SI Section S9).

Figures 6a-c show dI/dV maps at V_b = -0.08 V (associated with the below-Fermi partially populated LUMO) for MgPc "++" dimers with different Mg-Mg intermolecular distances $d_{c\text{-}c}$. For a small $d_{c\text{-}c}$ (Figures 5d, 6a), the below-Fermi partially populated LUMO associated with this map exhibits one nodal plane parallel to the Mg-Mg axis; this orbital is two-fold rotationally symmetric. As $d_{c\text{-}c}$ increases (Figures 6b, c), we observe the gradual appearance of a second nodal plane, perpendicular to the former; the orbital regains four-fold rotational symmetry and degeneracy, as for a single isolated MgPc.

To quantify this variation of LUMOs symmetry for MgPc in a "++" dimer, we defined from our dI/dV maps at V_b = -0.08 V (e.g., Figures 5b, d) an experimental spectroscopic asymmetry parameter $\alpha_{\mathrm{d}I/\mathrm{d}V}$:

$$\alpha_{\mathrm{d}I/\mathrm{d}V} = \frac{\iint |\mathcal{R}_{90°}[(\mathrm{d}I/\mathrm{d}V)_{\mathrm{bin}}(x,y,V_b=-0.08\ \mathrm{V})] - (\mathrm{d}I/\mathrm{d}V)_{\mathrm{bin}}(x,y,V_b=-0.08\ \mathrm{V})|\,\mathrm{d}x\,\mathrm{d}y}{\iint |\mathcal{R}_{90°}[(\mathrm{d}I/\mathrm{d}V)_{\mathrm{bin}}(x,y,V_b=-0.08\ \mathrm{V})] + (\mathrm{d}I/\mathrm{d}V)_{\mathrm{bin}}(x,y,V_b=-0.08\ \mathrm{V})|\,\mathrm{d}x\,\mathrm{d}y}$$

where $(\mathrm{d}I/\mathrm{d}V)_{\mathrm{bin}}(x,y,V_b=-0.08\ \mathrm{V})$ is the binarized dI/dV map as a function of tip position (x, y), and $\mathcal{R}_{90°}[(\mathrm{d}I/\mathrm{d}V)_{\mathrm{bin}}(x,y,V_b=-0.08\ \mathrm{V})]$ its 90° clockwise rotation around an axis perpendicular to the surface going through the Mg center (see SI section S11 for details). Figure 6g shows the calculated $\alpha_{\mathrm{d}I/\mathrm{d}V}$ for MgPc in "++" dimers with different values of $d_{c\text{-}c}$, yielding $\alpha_{\mathrm{d}I/\mathrm{d}V} = 1$ for the dimer with the smallest $d_{c\text{-}c}$ considered (~2 nm, i.e., most marked two-fold rotational symmetry, top panel, Figure 6a), decaying monotonically until $\alpha_{\mathrm{d}I/\mathrm{d}V} \to 0$ for $d_{c-c} > 3$ nm (i.e., four-fold rotational symmetry and degeneracy are recovered, as for single isolated MgPc).

Similarly, we calculated theoretical asymmetry parameters $\alpha_{\mathrm{DFT}}^{(\mathrm{Ag})}(d_{c-c})$ and $\alpha_{\mathrm{DFT}}^{(\mathrm{GP})}(d_{c-c})$ (red triangles and blue pentagons in Figure 6g) from DFT-simulated differential conductance maps for "++" dimers on Ag(100) and in the gas phase (GP), respectively, at a similar bias voltage related to the low energy LUMO (see Figures 6d-f, consistent with experimental data in Figures 6a-c, and SI Figure S20). The dependence of $\alpha_{\mathrm{d}I/\mathrm{d}V}$, $\alpha_{\mathrm{DFT}}^{(\mathrm{Ag})}$ and $\alpha_{\mathrm{DFT}}^{(\mathrm{GP})}$ on d_{c-c} can be fit with a decaying exponential function $\propto e^{-d_{c-c}/\lambda}$ (dashed curves in Figure 6g), with $\lambda_{\mathrm{d}I/\mathrm{d}V} = 0.5 \pm 0.2$ nm and $\lambda_{\mathrm{DFT}}^{(\mathrm{Ag})} = 0.6 \pm 0.1$ nm, showing good agreement between experiment and theory. For the gas phase "++" dimer, $\lambda_{\mathrm{DFT}}^{(\mathrm{GP})} = 0.09 \pm 0.02$ nm. That is, the range of the effectively attractive intermolecular interaction is significantly larger (> 5 times) on the noble metal surface than in the gas phase. Whilst $\alpha_{\mathrm{d}I/\mathrm{d}V}$, $\alpha_{\mathrm{DFT}}^{(\mathrm{Ag})} > 0$ for $d_{c-c} > 3$ nm, $\alpha_{\mathrm{DFT}}^{(\mathrm{GP})} \cong 0$ for $d_{c-c} \cong 2$ nm (see details in SI Figure S20).

3. Discussion

We considered several phenomena to explain the effective intermolecular attractive interaction that reduces the LUMO rotational symmetry observed both experimentally and in our DFT calculations. We exclude dipole-dipole or substrate-mediated (Friedel oscillations,

spin-spin) interactions as lacking consistency with our observations (see SI section S12 for details). Our DFT calculations of single MgPc on Ag(100) show significant spectral energy broadening and spatial delocalization of the LUMOs (when compared to those of the gas phase), due to hybridization with the substrate conduction electron states (SI Figure S18).

In order to provide a physical interpretation for the effective attractive interaction between MgPc's in a "++" dimer, we considered a simple model where we assume that: (i) the MgPc negative charge (resulting from the LUMOs partial filling via surface-to-molecule electron transfer) is screened by the Ag(100) conduction electrons which give rise to an image charge mitigating intermolecular Coulomb repulsion (similar to the case of other molecules with charge of same sign adsorbed on metal surfaces [52]); and (ii) two spatially delocalized orbitals [each resulting from the interaction between a LUMO and Ag(100) conduction electrons, and each associated with a different MgPc in a "++" dimer] can in turn hybridize, splitting the initially two-fold degenerate LUMOs into non-degenerate ones. In this model, for a "++" dimer with a specific $d_{\mathrm{c-c}}$, we considered four (two per MgPc) degenerate delocalized LUMO/Ag(100)-conduction-electron orbitals, that we first assumed non-interacting (see **Figure 7c**). We considered an effective one-electron Hamiltonian including two attractive central potentials ($\propto -1/r$) centered at each of the two Mg atoms of the "++" dimer. This effective Hamiltonian accounts for the attractive Coulomb interaction between negative electrons of one MgPc with positive nuclei of the other MgPc within a "++" dimer (see SI section S14). We then constructed new hybrid orbitals for the interacting "++" dimer via linear combination of the four, initially degenerate molecular orbitals (LCMO).

We used the two lowest energy LCMO-generated hybrid orbitals (labelled $|\varphi_1\rangle$ and $|\varphi_2\rangle$) to simulate the corresponding differential conductance maps (Figures 7a, b; see Methods and SI Figure S20). Up to $d_{\mathrm{c-c}} \cong 3$ nm, these maps exhibit a nodal plane parallel to the Mg-Mg dimer axis for $|\varphi_1\rangle$ (perpendicular to this axis for $|\varphi_2\rangle$), indicative of two-fold rotational symmetry. For $d_{\mathrm{c-c}} > \sim 3$ nm, these LCMO-generated orbitals show two nodal planes and a regained four-fold rotational symmetry (see SI Figure S20). This is consistent with our experimental and DFT-calculated (Figures 5 and 6) dI/dV maps.

These LCMO-derived differential conductance maps allowed us to calculate a spectroscopic asymmetry parameter $\alpha_{\mathrm{LCMO}}^{(\mathrm{Ag})}$ as a function of $d_{\mathrm{c-c}}$ (red hashes, Figure 6g). Exponential fitting of $\alpha_{\mathrm{LCMO}}^{(\mathrm{Ag})}(d_{\mathrm{c-c}})$ yielded $\lambda_{\mathrm{LCMO}}^{(\mathrm{Ag})} = 0.5 \pm 0.2$ nm, in close agreement with the experimental $\alpha_{\mathrm{d}I/\mathrm{d}V}(d_{\mathrm{c-c}})$ and DFT-derived $\alpha_{\mathrm{DFT}}^{(\mathrm{Ag})}(d_{\mathrm{c-c}})$ (see $\lambda_{\mathrm{d}I/\mathrm{d}V}$ and $\lambda_{\mathrm{DFT}}^{(\mathrm{Ag})}$ above). Using DFT-calculated LUMOs of gas phase MgPc as inputs to our LCMO model, we also performed the same procedure to calculate $\alpha_{\mathrm{LCMO}}^{(\mathrm{GP})}(d_{\mathrm{c-c}})$ (blue hashes in Figure 6g) that closely matches $\alpha_{\mathrm{DFT}}^{(\mathrm{GP})}$.

The quantitative agreement – for both dI/dV maps (Figures 7a, b) and $d_{\mathrm{c\text{-}c}}$-dependence of the spectroscopic asymmetry parameter α (Figure 6g) – between experiments, DFT and LCMO model validates the latter. This provides compelling evidence that the physical mechanism behind the observed LUMOs' symmetry reduction and lift of degeneracy consists of an

intermolecular hybridization-like process, with an increased spatial range (in comparison to the gas phase) given by the molecule-surface interaction and resulting LUMOs' delocalization.

The intermolecular hybridization should lower the energy of the molecular electronic system and further stabilize (in addition to screening by the metal substrate) the negative charge partially occupying the LUMOs. That is, the eigenenergy of the lowest-energy hybrid bonding orbital $|\varphi_1\rangle$ should be smaller than that of the degenerate LUMOs of non-interacting molecules. However, experimentally we observe no appreciable difference between the energy of the single isolated MgPc LUMOs and that of the "++" dimer $|\varphi_1\rangle$ (see Figure 5a). We attribute this to pinning of the LUMO just below the Fermi level given by the dipole formed at the interface between molecule and Ag(100) surface[53].

Substrate-mediated intermolecular hybridization has been reported previously for a binary closed-packed monolayer of ZnPc's on Ag(111)[54] where Zn-Zn distances are less than 2 nm, and hybrid ZnPc/Ag(111) orbitals were observed. In our case, substrate-mediated intermolecular hybridization clearly persists beyond Mg-Mg distances of ~3 nm, as shown by $\alpha_{\mathrm{d}I/\mathrm{d}V}$ (Figure 6g). Other STM and d*I*/d*V* STS studies on 3*d* TM-Pc's on Ag(100) have not reported any reduction of spatial symmetry of frontier orbitals due to intermolecular interactions[10]. The near-Fermi electronic structure of these systems is often dominated by features related to the (fully or partially occupied) transition metal *d*-orbitals[55] (e.g., zero-bias Kondo effect resonance), which can potentially hide or hinder the effect that we observed here. We claim that the MgPc/Ag(100) system, with its simpler electronic structure (only *s* and *p* molecular electrons; no near-Fermi d*I*/d*V* substrate features, e.g., Shockley surface state), and especially with its degenerate, partially populated LUMOs localized at the Pc periphery, allows us to isolate the long-range substrate-mediated intermolecular interaction (and resulting LUMOs lift of degeneracy and symmetry reduction) from other effects. Notably, $\alpha_{\mathrm{d}I/\mathrm{d}V}$ represents a highly sensitive real-space observable that (compared to, e.g., an energy-dependent LDOS measurement) lets us quantify the spatial dependence of this phenomenon.

4. Conclusion

We have studied the near-Fermi electronic structure of MgPc molecules on Ag(100). Our STM, d*I*/d*V* STS and ncAFM measurements, supported by DFT calculations, show that the LUMOs of single isolated molecules are partially populated and doubly degenerate, resulting in a four-fold rotationally symmetric near-Fermi occupied LDOS. An effective attractive intermolecular interaction between adsorbed MgPc's separated by up to ~3 nm can lift the LUMOs degeneracy and break the rotational spatial symmetry of the near-Fermi molecular states. We explain this interaction within a first-order simplified model (LCMO) that accounts for an effective long-range hybridization between partially populated LUMOs, delocalized due to the adsorption on the noble metal surface. Our study highlights how interactions between molecules on metal surfaces can extend over several nm's due to delocalization of molecular electronic states, significantly altering energy degeneracies and

spatial symmetries of the latter. This can have severe effects on (and provide opportunities for control of) electronic properties of molecule-metal interfaces in solid-state systems where functionality depends on such symmetries, such as dipole matrix elements in optoelectronics or non-equilibrium Green's functions in molecular electronics[56].

5. Experimental and Theoretical Methods

Sample preparation:

MgPc molecules (Sigma Aldrich) were deposited in ultrahigh vacuum (UHV) from the gas-phase (sublimation temperature: 340°C) onto a clean Ag(100) surface (Mateck GmbH) maintained at room temperature. The Ag(100) was prepared by repeated cycles of Ar^+ sputtering and annealing (450°C). Molecules were deposited at sub-monolayer coverages (~10% of 1 monolayer). The base pressure was below 3 x 10^{-9} mbar during depositions.

STM & dI/dV STS measurements:

All STM and dI/dV STS measurements were performed at 4.6 K in UHV (< 1 x 10^{-10} mbar) with an Ag-terminated Pt/Ir tip. Topographic STM images were acquired in constant-current mode. Differential conductance dI/dV spectra (Figures 3, 4a, 5a) were obtained by averaging multiple $I(V)$ curves (at least 10) and numerical derivation. All dI/dV maps in main text and SI (except SI Figure S7b; see corresponding figure caption) were acquired using a multi-pass (MP) approach (see SI Section S7). This technique consists of: (i) acquiring a constant-current STM topographic profile along a scanning line (we used a setpoint V_b = -2.5 V, I_t = 100 pA, at a scanning speed of 3 nm s^{-1}), and (ii) recording dI/dV with a lock-in amplifier (bias voltage modulation amplitude: 20 mV; frequency: 665 Hz) while scanning (speed: 1.5 nm s^{-1}) the same line and following the same constant-current STM topographic profile as in (i), with the tip approached of an additional 150 pm towards the sample; (iii) finally, repeating this procedure sequentially for each scanned line of the map. This approach has the benefit of minimizing variations of dI/dV due to variations in STM apparent topography.

CO functionalisation:

All of our ncAFM imaging data (and STM in SI Figure S1) were acquired with a tip (Pt/Ir) functionalized with a carbon monoxide (CO) molecule at its apex. Such tip functionalization was achieved by dosing CO gas into the UHV chamber (5 x 10^{-8} mbar for ~10 s) with the Ag(100) sample held at 8 K, placing the tip above a CO molecule on bare Ag(100) with an STM bias voltage of 3 mV, and approaching the tip towards the surface (feedback off) until the tunneling current reaches ~5 nA and then decreases suddenly due to a CO molecule being picked-up.

NcAFM measurements:

Non-contact AFM measurements were performed at 4.6 K in UHV (< 1 x 10^{-10} mbar) using a qPlus tuning fork, in frequency modulation mode (resonance frequency $f \cong 29$ kHz; spring constant $k \cong 1800$ N m^{-1}), with a CO-functionalized Pt/Ir tip. Frequency-shift ncAFM maps (Figures 2a, b) were acquired at constant height, with a 60 pm amplitude oscillation, and with the tip approached 40 pm towards the surface with respect to the STM setpoint V_b = 0.02 V, I_t = 5 pA on bare Ag. No bias voltage was applied during ncAFM map acquisition. NcAFM maps were smoothed by convolution with a Gaussian function, followed by a Laplace edge detection and a minimum filter.[44]

DFT calculations:

We performed DFT calculations for gas-phase MgPc and MgPc on Ag(100) using the SIESTA[57] simulation tool with periodic boundary conditions, Troullier-Martins norm-conserving pseudopotentials (with relativistic corrections[58] for Ag) and the RPBE exchange-correlation[59] functional with van der Waals corrections (Grimme's method)[60]. Kohn-Sham orbitals were represented by a DZP basis set with an energy shift of 0.01 and 0.02 Ry for the gas phase and Ag(100), respectively. The total electron charge density was represented on a real space grid corresponding to a mesh cut-off of 300 Ry. The Ag(100) surface was modelled with a 5-layer slab of Ag atoms and a vacuum gap of 7 layers. The behaviour of a single adsorbed MgPc molecule was modelled on a 8×8 lateral supercell, while lateral supercells of 11×9 and 13×9 were used for MgPc "++" dimer systems. Reciprocal space *k*-points were sampled on a $1 \times 1 \times 1$ Monkhorst-Pack grid[61] for all slab systems. A lattice constant of 4.16 Å was used for bulk Ag. Structural optimization was performed for a single MgPc (Figure 2c) and for a "++" dimer with $d_{\text{c-c}} \cong 2.0$ nm (Figure 2d), by relaxing the atoms of molecules and of the Ag(100) upper 3 layers, such that the Cartesian components of forces on relaxing atoms were reduced below 0.02 eV/Å. Gas-phase "++" dimers (used to calculate $\alpha_{\text{DFT}}^{(\text{GP})}$ in Figure 6g) were structurally relaxed with the positions of center Mg atoms fixed. Subsequent calculations for "++" dimers adsorbed on Ag(100) with other values of $d_{\text{c-c}}$ (used to calculate $\alpha_{\text{DFT}}^{(\text{Ag})}$ in Figure 6g) were performed by assuming a flat molecular structure, with $d_{\text{c-c}}$ varied by moving MgPc molecules to different hollow sites of the substrate (maintaining the same adsorption angle). These systems were constructed using the atomic positions of gas-phase MgPc and bare Ag(100), with adsorption heights and substrate interlayer spacings set to their respective averages found from the fully relaxed adsorbed "++" dimer with $d_{\text{c-c}} \cong 2.0$ nm, without further structural relaxation. This is justified by the negligible distortions of the computed relaxed structure of single MgPc and "++" dimer, in agreement with experimental ncAFM imaging (Figure 2a, b).

We used the DFT-calculated one-electron Kohn-Sham orbitals ψ_ν (with eigenenergy E_ν) to simulate theoretical differential conductance (d*I*/d*V*) STS maps (Figure 5f-i; S7d-f, S16c, S20 in SI) according to the Tersoff-Hamann approximation, where first-order perturbation theory is applied with the assumption of spherically symmetric tip states[62, 63]:

$$\frac{\partial I}{\partial V}(x, y, z_0, V) \propto \sum_{\nu} |\psi_\nu(\vec{r}_0)|^2 \cdot \delta\big(E_\nu - E_f + eV\big)$$

where $\psi_\nu(\vec{r}_0)$ is a single-electron Kohn-Sham wavefunction with eigenenergy E_ν, $\vec{r}_0 = (x, y, z_0)$ is the position of the tip (z_0: tip-sample distance, where $z = 0$ corresponds to the molecular plane; *xy* plane is parallel to surface and molecular plane), *V* is the bias voltage of interest and E_f the Fermi energy.

We first numerically evaluated the single-electron Kohn-Sham orbitals $\psi_\nu(x, y, z_0)$ at a reference *xy* plane sufficiently close to atoms such that wavefunctions are defined within numerical error, yet sufficiently far such that the potential does not diverge nor varies steeply.

We chose a distance of $z_0 = 1.7$ Å above the molecular plane. We then Fourier expanded $\psi_v(x, y, z_0)$ within this reference plane (consistent with the DFT calculations periodic boundary conditions):

$$\psi_{n,\vec{k}}(x, y, z_0) = \sum_{\vec{G}} a_{\vec{k},\vec{G}}(z_0) \exp\left(i\left[(k_x + G_x)x + \left(k_y + G_y\right)y\right]\right)$$

and substituted this Fourier expansion into the vacuum Schrödinger equation[64]:

$$-\frac{\hbar^2}{2m}\nabla^2\psi_{n,\vec{k}}(x, y, z) = \left(E_{n,\vec{k}} - E_{\mathrm{vac}}\right)\psi_{n,\vec{k}}(x, y, z)$$

where E_{vac} is the vacuum energy, yielding

$$a_{\vec{k},\vec{G}}(z) = a_{\vec{k},\vec{G}}(z_0) \exp\left(-\lambda_{\vec{k},\vec{G}}(z - z_0)\right)$$

with

$$\lambda_{\vec{k},\vec{G}} = \sqrt{\left(\vec{k} + \vec{G}\right)^2 - \frac{2m}{\hbar^2}(E_{n,\vec{k}} - E_{\mathrm{vac}})}$$

where $\vec{k} = (k_x, k_y)$ and $\vec{G} = (G_x, G_y)$. This allows us to evaluate $\psi_{n,\vec{k}}(x, y, z_0)$ at any height z_0 with respect to the reference plane. The theoretically calculated dI/dV maps shown throughout main text and SI (as well as the derived spectroscopic asymmetry parameters $\alpha_{\mathrm{DFT}}^{(\mathrm{Ag})}$, $\alpha_{\mathrm{DFT}}^{(\mathrm{GP})}$, $\alpha_{\mathrm{LCMO}}^{(\mathrm{Ag})}$, $\alpha_{\mathrm{LCMO}}^{(\mathrm{GP})}$) correspond to a distance of 4.3 Å above the molecular plane (i.e., 2.6 Å above the aforementioned reference plane).

Supporting Information

Supporting Information is available from the Wiley Online Library or from the author.

Acknowledgements
A.S. acknowledges support from the Australian Research Council (ARC) Future Fellowship scheme (FT150100426). M.C. acknowledges support from the Monash Centre of Atomically Thin Materials (MCATM), and the ARC Centre of Excellence in Future Low-Energy Electronics Technologies (FLEET). The computational resources for this work were provided by the National Computing Infrastructure (NCI) and Pawsey Supercomputing Center through National Computational Merit Allocation Scheme (NCMAS). S.G., L.H. and M.U. acknowledge useful discussions with Charles Hill (The University of Melbourne).

Author Contributions:
M.C., J.H., C.K. and A.S. designed and performed all experiments, and analysed and interpreted all data. M.U. supervised the theoretical calculations with input from L.C.L.H. S.G. performed the DFT calculations and theoretical simulations of dI/dV STS maps. M.C.

performed the LCMO calculations with input from S.G. M.C., J.H., S.G., M.U. and A.S. wrote the manuscript. All authors discussed the results and contributed to the final manuscript.

Conflict of Interest

The authors have no financial or commercial conflicts of interest to declare.

Received: ((will be filled in by the editorial staff))
Revised: ((will be filled in by the editorial staff))
Published online: ((will be filled in by the editorial staff))

References

1. Lu, H.; Zhang, X. P., *Chem. Soc. Rev.* **2011,** *40*, 1899-1909.
2. Sorokin, A. B., *Chem. Rev.* **2013,** *113*, 8152-8191.
3. Schumann, S.; Hatton, R. A.; Jones, T. S., *J. Phys. Chem. C* **2011,** *115*, 4916-4921.
4. Walter, M. G.; Rudine, A. B.; Wamser, C. C., *J. Porphyrins Phthalocyanines* **2010,** *14*, 759-792.
5. Martinez-Diaz, M. V.; de la Torre, G.; Torres, T., *Chem. Commun.* **2010,** *46*, 7090-7108.
6. Xu, H.; Chen, R.; Sun, Q.; Lai, W.; Su, Q.; Huang, W.; Liu, X., *Chem. Soc. Rev.* **2014,** *43*, 3259-3302.
7. Hohnholz, D.; Steinbrecher, S.; Hanack, M., *J. Mol. Struct.* **2000,** *521*, 231-237.
8. Li, B.; Li, J.; Fu, Y.; Bo, Z., *J. Am. Chem. Soc.* **2004,** *126*, 3430-3431.
9. Tsukahara, N.; Noto, K.-i.; Ohara, M.; Shiraki, S.; Takagi, N.; Takata, Y.; Miyawaki, J.; Taguchi, M.; Chainani, A.; Shin, S.; Kawai, M., *Phys. Rev. Lett.* **2009,** *102*, 167203.
10. Mugarza, A.; Robles, R.; Krull, C.; Korytár, R.; Lorente, N.; Gambardella, P., *Phys. Rev. B* **2012,** *85*, 155437.
11. Wende, H.; Bernien, M.; Luo, J.; Sorg, C.; Ponpandian, N.; Kurde, J.; Miguel, J.; Piantek, M.; Xu, X.; Eckhold, P., *Nat. Mater.* **2007,** *6*, 516.
12. Rosei, F.; Schunack, M.; Naitoh, Y.; Jiang, P.; Gourdon, A.; Laegsgaard, E.; Stensgaard, I.; Joachim, C.; Besenbacher, F., *Prog. Surf. Sci.* **2003,** *71*, 95-146.
13. de la Torre, G.; Claessens, C. G.; Torres, T., *Chem. Commun.* **2007**, 2000-2015.
14. Bohrer, F. I.; Colesniuc, C. N.; Park, J.; Ruidiaz, M. E.; Schuller, I. K.; Kummel, A. C.; Trogler, W. C., *J. Am. Chem. Soc.* **2009,** *131*, 478-485.
15. Zhang, J. L.; Zhong, J. Q.; Lin, J. D.; Hu, W. P.; Wu, K.; Xu, G. Q.; Wee, A. T. S.; Chen, W., *Chem. Soc. Rev.* **2015,** *44*, 2998-3022.
16. Niu, T.; Li, A., *J. Phys. Chem. Lett.* **2013,** *4*, 4095-4102.
17. Auwärter, W.; Écija, D.; Klappenberger, F.; Barth, J. V., *Nat. Chem.* **2015,** *7*, 105.
18. Gottfried, J. M., *Surf. Sci. Rep.* **2015,** *70*, 259-379.

19. Liao, M.-S.; Scheiner, S., *J. Chem. Phys.* **2001,** *114*, 9780-9791.
20. Kezilebieke, S.; Amokrane, A.; Abel, M.; Bucher, J.-P., *J. Phys. Chem. Lett.* **2014,** *5* (18), 3175-3182.
21. Gopakumar, T. G.; Brumme, T.; Kröger, J.; Toher, C.; Cuniberti, G.; Berndt, R., *J. Phys. Chem. C* **2011,** *115*, 12173-12179.
22. Masaki, T.; Hirokazu, T., *Jpn. J. Appl. Phys.* **2005,** *44*, 5332.
23. Chen, F.; Chen, X.; Liu, L.; Song, X.; Liu, S.; Liu, J.; Ouyang, H.; Cai, Y.; Liu, X.; Pan, H.; Zhu, J.; Wang, L., *App. Phys. Lett.* **2012,** *100*, 081602.
24. Chang, S.-H.; Kuck, S.; Brede, J.; Lichtenstein, L.; Hoffmann, G.; Wiesendanger, R., *Phys. Rev. B* **2008,** *78*, 233409.
25. Snezhkova, O.; Lüder, J.; Wiengarten, A.; Burema, S. R.; Bischoff, F.; He, Y.; Rusz, J.; Knudsen, J.; Bocquet, M.-L.; Seufert, K.; Barth, J. V.; Auwärter, W.; Brena, B.; Schnadt, J., *Phys. Rev. B* **2015,** *92*, 075428.
26. Kügel, J.; Hsu, P.-J.; Böhme, M.; Schneider, K.; Senkpiel, J.; Serrate, D.; Bode, M.; Lorente, N., *Phys. Rev. Lett.* **2018,** *121*, 226402.
27. Uhlmann, C.; Swart, I.; Repp, J., *Nano Lett.* **2013,** *13*, 777-780.
28. Krull, C.; Robles, R.; Mugarza, A.; Gambardella, P., *Nat. Mater.* **2013,** *12*, 337-343.
29. Andjelkovic, L.; Stepanovic, S.; Vlahovic, F.; Zlatar, M.; Gruden, M., *Phys. Chem. Chem. Phys.* **2016,** *18*, 29122-29130.
30. Tóbik, J.; Tosatti, E., *J. Mol. Struct.* **2007,** *838*, 112-115.
31. Zandvliet, H. J. W.; van Houselt, A., *Annu. Rev. Anal. Chem.* **2009,** *2*, 37-55.
32. Mugarza, A.; Lorente, N.; Ordejón, P.; Krull, C.; Stepanow, S.; Bocquet, M. L.; Fraxedas, J.; Ceballos, G.; Gambardella, P., *Phys. Rev. Lett.* **2010,** *105*, 115702.
33. de Oteyza, D. G.; El-Sayed, A.; Garcia-Lastra, J. M.; Goiri, E.; Krauss, T. N.; Turak, A.; Barrena, E.; Dosch, H.; Zegenhagen, J.; Rubio, A.; Wakayama, Y.; Ortega, J. E., *J. Chem. Phys.* **2010,** *133*, 214703.
34. Mugarza, A.; Krull, C.; Robles, R.; Stepanow, S.; Ceballos, G.; Gambardella, P., *Nat. Commun.* **2011,** *2*, 490.
35. Perera, U. G. E.; Kulik, H. J.; Iancu, V.; Dias da Silva, L. G. G. V.; Ulloa, S. E.; Marzari, N.; Hla, S. W., *Phys. Rev. Lett.* **2010,** *105*, 106601.
36. Fernández-Torrente, I.; Franke, K. J.; Pascual, J. I., *Phys. Rev. Lett.* **2008,** *101*, 217203.
37. Colonna, S.; Mattioli, G.; Alippi, P.; Amore Bonapasta, A.; Cricenti, A.; Filippone, F.; Gori, P.; Paoletti, A. M.; Pennesi, G.; Ronci, F.; Zanotti, G., *J. Phys. Chem. C* **2014,** *118*, 5255-5267.
38. Masuda, T., *Photosynth. Res.* **2008,** *96*, 121-143.
39. Elemans, J. A. A. W.; van Hameren, R.; Nolte, R. J. M.; Rowan, A. E., *Adv. Mater.* **2006,** *18*, 1251-1266.

40. Peltekis, N.; Holland, B. N.; Krishnamurthy, S.; McGovern, I. T.; Poolton, N. R. J.; Patel, S.; McGuinness, C., *J. Am. Chem. Soc.* **2008,** *130*, 13008-13012.
41. Miwa, K.; Imada, H.; Kawahara, S.; Kim, Y., *Phys. Rev. B* **2016,** *93*, 165419.
42. Lin, X.; Nilius, N., *J. Phys. Chem. C* **2008,** *112*, 15325-15328.
43. Patera, L. L.; Queck, F.; Scheuerer, P.; Moll, N.; Repp, J., *Phys. Rev. Lett.* **2019,** *123*, 016001.
44. Krull, C.; Castelli, M.; Hapala, P.; Kumar, D.; Tadich, A.; Capsoni, M.; Edmonds, M. T.; Hellerstedt, J.; Burke, S. A.; Jelinek, P.; Schiffrin, A., *Nat. Commun.* **2018,** *9*, 3211.
45. Gross, L.; Mohn, F.; Moll, N.; Liljeroth, P.; Meyer, G., *Science* **2009,** *325*, 1110-1114.
46. Pavel, J., *J. Phys.: Condens. Matter* **2017,** *29*, 343002.
47. van der Lit, J.; Di Cicco, F.; Hapala, P.; Jelinek, P.; Swart, I., *Phys. Rev. Lett.* **2016,** *116*, 096102.
48. de la Torre, B.; Švec, M.; Hapala, P.; Redondo, J.; Krejčí, O.; Lo, R.; Manna, D.; Sarmah, A.; Nachtigallová, D.; Tuček, J.; Błoński, P.; Otyepka, M.; Zbořil, R.; Hobza, P.; Jelínek, P., *Nat. Commun.* **2018,** *9*, 2831.
49. Aroca, R.; Zeng, Z. Q.; Mink, J., *J. Phys. Chem. Solids* **1990,** *51*, 135-139.
50. Zhang, X.; Zhang, Y.; Jiang, J., *Spectrochim. Acta, Part A* **2004,** *60*, 2195-2200.
51. Tang, W.; Sanville, E.; Henkelman, G., *J. Phys.: Condens. Matter* **2009,** *21*, 084204.
52. Schiffrin, A.; Reichert, J.; Pennec, Y.; Auwärter, W.; Weber-Bargioni, A.; Marschall, M.; Dell'Angela, M.; Cvetko, D.; Bavdek, G.; Cossaro, A.; Morgante, A.; Barth, J. V., *J. Phys. Chem. C* **2009,** *113*, 12101-12108.
53. Braun, S.; Salaneck, W. R.; Fahlman, M., *Adv. Mater.* **2009,** *21*, 1450-1472.
54. Calzolari, A.; Jin, w.; Reutt-Robey, J. E.; Buongiorno Nardelli, M., *J. Phys. Chem. C* **2010,** *114*, 1041-1045.
55. Kügel, J.; Karolak, M.; Senkpiel, J.; Hsu, P.-J.; Sangiovanni, G.; Bode, M., *Nano Lett.* **2014,** *14*, 3895-3902.
56. Cohen, G.; Galperin, M., *J. Chem. Phys.* **2020,** *152*, 090901.
57. Soler, J. M.; Artacho, E.; Gale, J. D.; Garcìa, A.; Junquera, J.; Ordejn, P.; Sànchez-Portal, D., *J. Phys.: Condens. Matter* **2002,** *14*, 2745.
58. Rivero, P.; García-Suárez, V. M.; Pereñiguez, D.; Utt, K.; Yang, Y.; Bellaiche, L.; Park, K.; Ferrer, J.; Barraza-Lopez, S., *Comput. Mater. Sci.* **2015,** *98*, 372-389.
59. Hammer, B.; Hansen, L. B.; Nørskov, J. K., *Phys. Rev. B* **1999,** *59*, 7413.
60. Grimme, S., *J. Comput. Chem.* **2006,** *27*, 1787-1799.
61. Monkhorst, H. J.; Pack, J. D., *Phys. Rev. B* **1976,** *13*, 5188.
62. Tersoff, J.; Hamann, D. R., *Phys. Rev. B* **1985,** *31*, 805.
63. Bardeen, J., *Phys. Rev. Lett.* **1961,** *6*, 57.
64. Rohlfing, M.; Temirov, R.; Tautz, F. S., *Phys. Rev. B* **2007,** *76*, 115421.

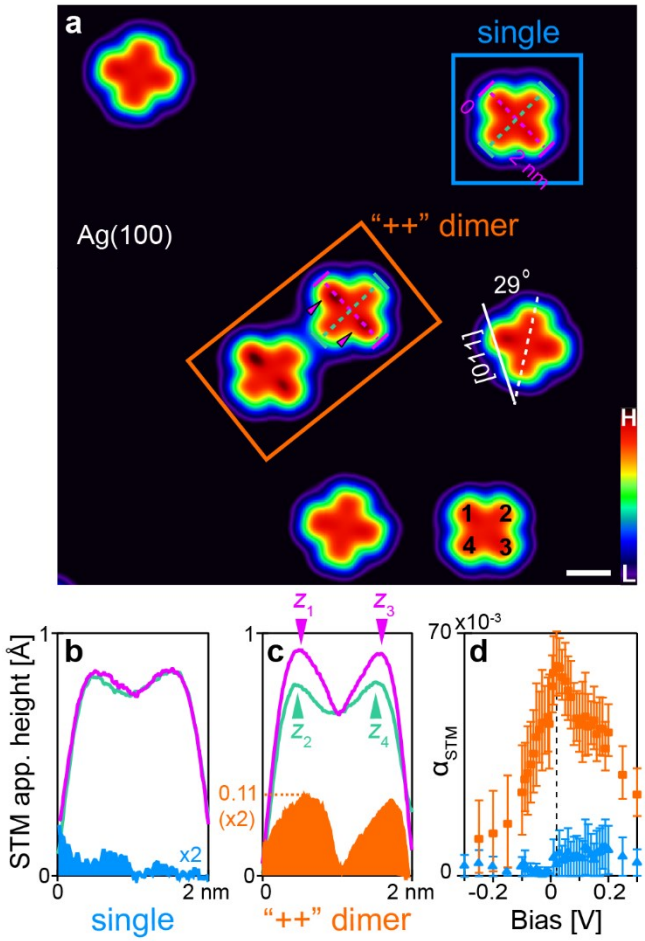

Figure 1. Symmetry reduction of STM apparent topography induced by nearest-neighbour MgPc on Ag(100). (a) Constant-current STM image (V_b = 0.02 V, I_t = 5 pA) of MgPc molecules on Ag(100). Single isolated molecules (blue frame) show four-fold rotational symmetry. Molecules with a neighbouring MgPc, with collinear isoindole-isoindole axes ("++" dimer; orange frame; Mg-Mg distance: $d_{c\text{-}c}$ = 2.29 nm) appear two-fold symmetric. Scale bar: 1 nm. (b) STM apparent height profiles (solid magenta and green curves), along the two orthogonal isoindole-isoindole axes [dashed magenta and green lines (a)] for a single molecule. Filled blue curve corresponds to the difference between solid magenta and green curves. (c) Same as (b), for a "++" dimer. Filled orange curve corresponds to the difference between solid magenta and green curves. (d) STM topographic asymmetry parameter $\alpha_{STM} = \frac{|(z_1+z_3)-(z_2+z_4)|}{(z_1+z_3+z_2+z_4)}$, for single molecule (blue) and molecule in "++"dimer (orange; $d_{c\text{-}c}$ = 2.1 nm), as a function of STM bias voltage, where z_j (j = 1, …, 4) is the maximum STM apparent height for each of the four isoindole groups, and $z_1 > z_3 > z_2 > z_4$

[see bottom right MgPc in (a) for labelling]. Error bars were determined by calculating extremal values of α_{STM} : $\alpha_{\mathrm{STM,max}} = \frac{z_1 - z_4}{z_1 + z_4}$; $\alpha_{\mathrm{STM,min}} = \frac{z_3 - z_2}{z_3 + z_2}$.

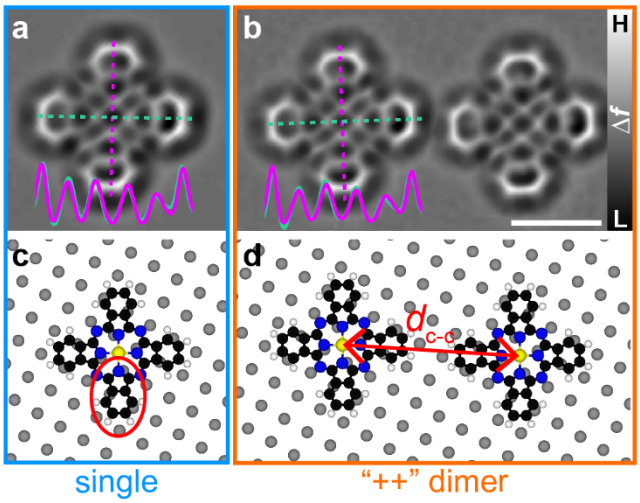

Figure 2. Morphology of single and "++" dimer MgPc's on Ag(100): ncAFM and DFT. (a) Constant-height, Laplace-filtered ncAFM image [tip approached 40 pm with respect to STM setpoint V_b = 0.02 V, I_t = 5 pA on bare Ag(100); CO-functionalized tip] of single molecule. (b) Same as (a), for "++" dimer ($d_{c\text{-}c}$ = 2.03 nm). Insets: ncAFM apparent height profiles along isoindole-isoindole axes. (c) DFT-calculated relaxed adsorption geometry of single molecule. Yellow: Mg; black: C; blue: N; white: H; grey: Ag. Isoindole unit circled in red. Only top Ag layer is shown for clarity. (d) Same as (c), for "++" dimer ($d_{c\text{-}c}$ = 1.98 nm).

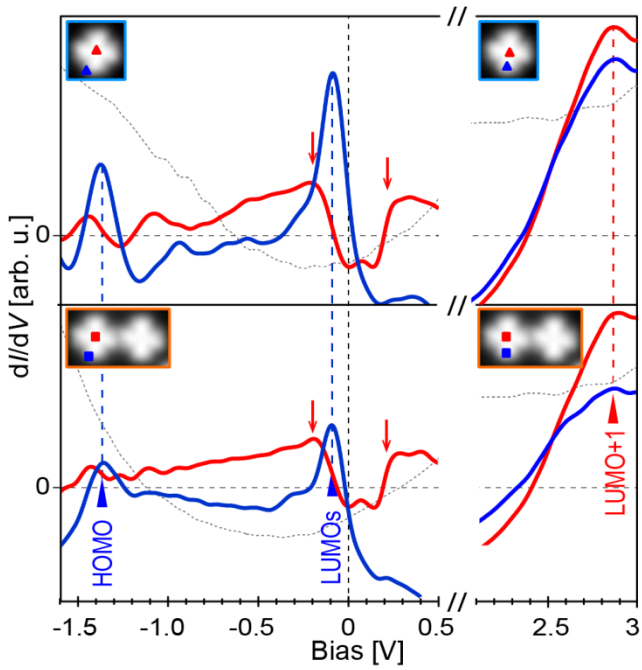

Figure 3. Electronic structure of single MgPc and MgPc of a "++" dimer on Ag(100). dI/dV spectra acquired on the phthalocyanine (Pc) ligand (blue) and Mg center (red) for single MgPc (top panel) and "++" dimer (bottom). dI/dV spectra were background subtracted using the dI/dV curve on bare Ag (dashed grey curve). Setpoints: V_b = -2 V, I_t = 3 nA for data from -1.6 to 0.5 V; V_b = 3 V, I_t = 50 pA for data from 2.1 to 3 V. Blue and red triangular ticks indicate features related to the gas-phase HOMO, the two-fold degenerate gas-phase LUMOs [partially filled here on Ag(100)] and higher energy unoccupied states of gas-phase MgPc. Red arrows indicate near-Fermi features related to molecular vibrational modes. Insets: STM images of single MgPc (top) and "++" dimer (bottom).

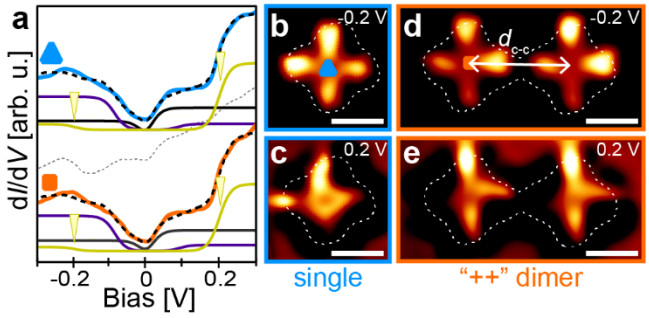

Figure 4. Near-Fermi d*I*/d*V* STS: vibrational modes. (a) d*I*/d*V* point spectra on Mg center for single MgPc (blue) and MgPc "++" dimer (orange; $d_{c\text{-}c}$ = 2.0 nm). Tip was approached 100 pm towards the sample, with respect to the STM setpoint V_b = -2.5 V, I_t = 400 pA. Spectra were fit (black dashed curve) with a sum of Fermi-Dirac distributions (solid yellow, black, purple curves) and of attenuated reference bare Ag(100) spectrum (SI section S6 for details). (b)-(e) d*I*/d*V* maps at V_b = ± 0.2 V for single MgPc (blue) and "++" dimer (orange). White dashed outlines indicate molecule STM topographic contour (V_b = -2.5 V, I_t = 100 pA). Scale bars: 1 nm.

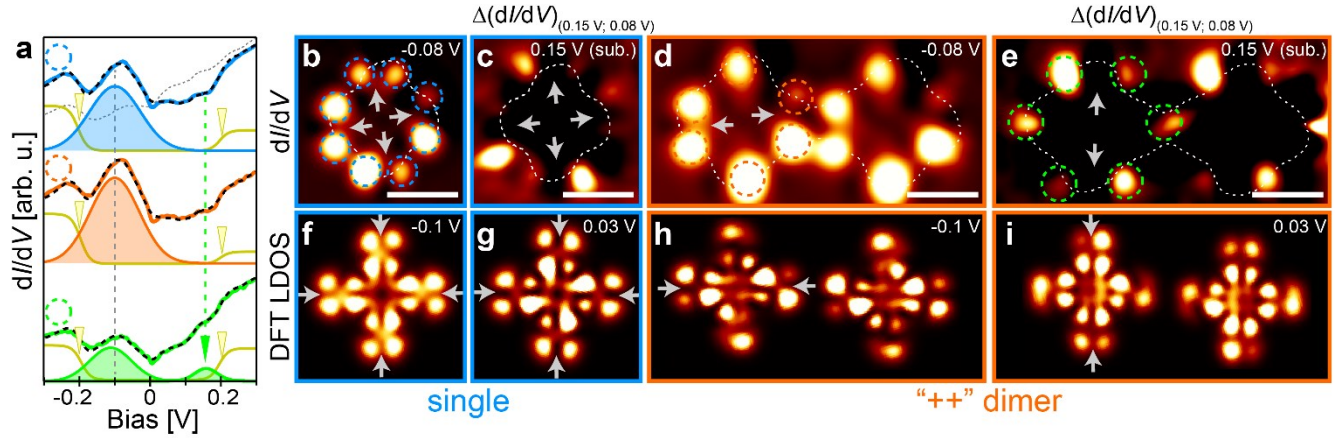

Figure 5. Near-Fermi electronic structure: symmetry breaking and lift of LUMO degeneracy. (a) d*I*/d*V* point spectra (solid blue, orange, green curves) averaged over peripheral ligand regions indicated by dashed circles in (b), (d) and (e). Spectra were fit (black dashed curves) with a sum of Fermi-Dirac distributions (yellow curves), Gaussian peaks (filled curves) and an attenuated reference bare Ag(100) spectrum (grey dashed curve). Spectra were acquired with the same tip and parameters as in Figure 4 (tip approached 100 pm towards sample, with respect to STM setpoint V_b = -2.5 V, I_t = 400 pA). (b) - (e) d*I*/d*V* maps at V_b = -0.08 and 0.15 V for single MgPc and "++" dimer. Maps acquired at 0.15 V (c, e) were subtracted by maps acquired at 0.08 V [i.e., $\Delta(dI/dV)_{(0.15\ V;\ 0.08\ V)} = (dI/dV)_{0.15\ V} - (dI/dV)_{0.08\ V}$], to minimize inelastic

contributions of molecular vibrational modes and emphasize elastic features of LUMOs. Grey arrows indicate orbital nodal planes. (f) - (i) Corresponding DFT-calculated differential conductance maps (Methods). White dashed outlines indicate molecule STM topographic contour (V_b = -2.5 V, I_t = 100 pA). Scale bars: 1 nm.

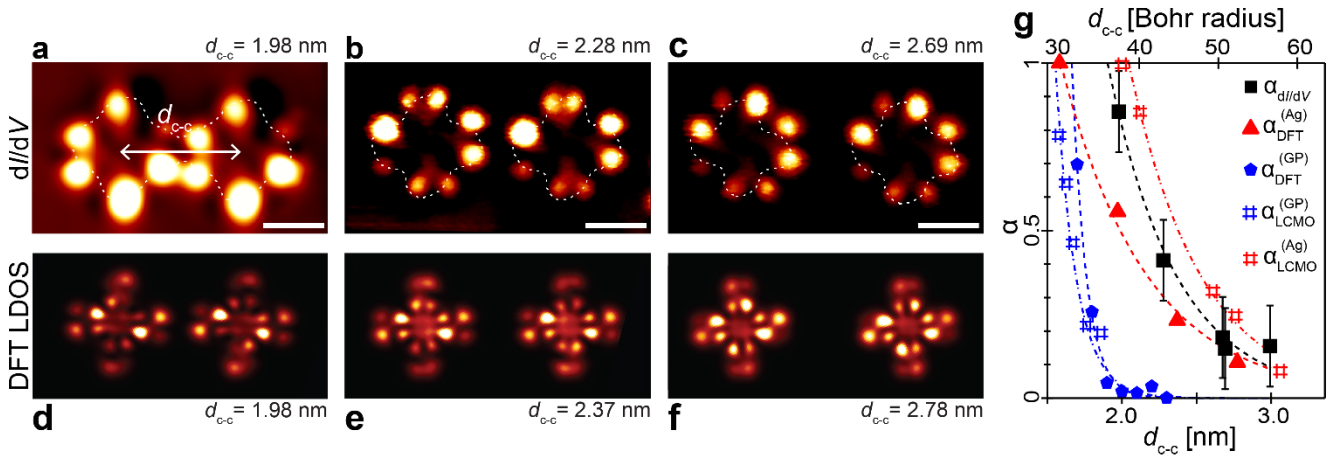

Figure 6. Distance-dependence of LUMO symmetry and spectroscopic asymmetry parameter for MgPc in "++" dimer. (a) – (c) dI/dV maps at V_b = -0.08 V of "++" dimers with different intermolecular separations $d_{c\text{-}c}$. White dashed outlines: molecule STM topographic (V_b = -2.5 V, I_t = 100 pA). Scale bars: 1 nm. (d) – (f) Corresponding DFT-simulated dI/dV maps (Methods). (g) Spectroscopic asymmetry parameters α as a function of intermolecular center-center distance $d_{c\text{-}c}$. Black squares: experimental $\alpha_{dI/dV}$ retrieved from dI/dV maps at V_b = -0.08 V (see SI sections S10 and S11); error bars correspond to $\alpha_{dI/dV}$ calculated for a single isolated MgPc (which differs slightly from zero due to tip asymmetries; see SI). Red triangles (blue pentagons): $\alpha_{DFT}^{(Ag)}$ ($\alpha_{DFT}^{(GP)}$) extracted from DFT-simulated dI/dV maps of "++" dimer on Ag(100) (in gas-phase, respectively); see Methods and SI Figure S19. Red (blue) hashes: $\alpha_{LCMO}^{(Ag)}$ ($\alpha_{LCMO}^{(GP)}$) extracted from Linear Combination of Molecular Orbitals (LCMO) model for "++" dimer on Ag(100) (in gas-phase, respectively). Dashed curves: decaying exponential fits.

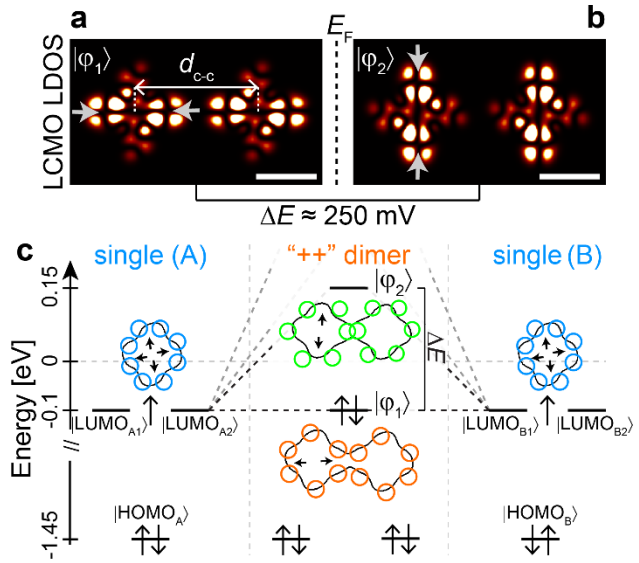

Figure 7. Long-range molecule-molecule hybridization mediated by Ag(100) substrate. (a), (b) Calculated differential conductance maps (see Methods) corresponding to the two lowest energy hybrid orbitals φ_1 and φ_2 generated with our LCMO model (see SI section S14) for a "++" dimer ($d_{c\text{-}c} \cong 2.0$ nm). Grey arrows indicate nodal planes. Scale bars: 1 nm. (c) Energy level diagram for single MgPc's *A* and *B* (left and right), each with doubly degenerate, partially occupied LUMOs, and a "++" dimer (center) with non-degenerate, occupied and unoccupied hybrid orbitals. Blue, orange and green contours represent spatial distributions of experimental d*I*/d*V* maps in Figure 5b, d, e, respectively. Solid black curves: corresponding STM molecular contours (V_b = -2.5 V, I_t = 100 pA; Figure 5).

Table of Contents:

Long-Range Surface-Assisted Molecule-Molecule Hybridization

Marina Castelli, Jack Hellerstedt, Cornelius Krull, Spiro Gicev, Lloyd C.L. Hollenberg, Muhammad Usman, Agustin Schiffrin

On a silver surface, magnesium phthalocyanine molecules undergo a perturbation of their electronic structure as a result of an attractive interaction with their nearest-neighbors. Quantitative agreement with supporting theoretical modelling indicates that this interaction consists of multiple-nanometer-range intermolecular hybridization enabled by the underlying substrate. These observations offer new possibilities to control electronic properties for engineered nanomaterials.